Accepted Manuscript

Zn defective ZnCo2O4 nanorods as high capacity anode for lithium ion batteries

Marilena Carbone

PII: S1572-6657(18)30125-5
DOI: doi:10.1016/j.jelechem.2018.02.035
Reference: JEAC 3887

To appear in: *Journal of Electroanalytical Chemistry*

Received date: 15 December 2017
Revised date: 23 January 2018
Accepted date: 14 February 2018

Please cite this article as: Marilena Carbone , Zn defective ZnCo2O4 nanorods as high capacity anode for lithium ion batteries. The address for the corresponding author was captured as affiliation for all authors. Please check if appropriate. Jeac(2017), doi:10.1016/j.jelechem.2018.02.035

This is a PDF file of an unedited manuscript that has been accepted for publication. As a service to our customers we are providing this early version of the manuscript. The manuscript will undergo copyediting, typesetting, and review of the resulting proof before it is published in its final form. Please note that during the production process errors may be discovered which could affect the content, and all legal disclaimers that apply to the journal pertain.

ACCEPTED MANUSCRIPT

Zn defective $ZnCo_2O_4$ nanorods as high capacity anode for lithium ion batteries

Marilena Carbone*

Dept. of Chemical Science and Technologies, University of Rome Tor Vergata, Via della Ricerca Scientifica, 1 00133 Roma, Italy

* Corresponding author: marilena.carbone@roma2.infn.it

Abstract

Zn defective $ZnCo_2O_4$ nanorods, made of nanoparticles in the size range 10-20 nm, re-arranged in tubular superstructures are investigated as lithium ion battery anode material. They are prepared by a step-wise synthetic procedure, consisting of a co-precipitation with a chelating agent assisted by a dispersing agent, autoclave treatment and subsequent calcination. Zn vacancies are, then, introduced by an alkaline etching procedure. An extensive structural and morphological characterization is performed by thermogravimetry coupled with differential thermal analysis, X-ray diffraction, X-ray photoelectron spectroscopy, surface area measurements, inductively coupled plasma atomic emission spectroscopy, scanning and transmission electron microscopies. The defective $ZnCo_2O_4$ nanorods-based anode exhibits a high specific capacity, i.e. 1398.8 mAh g^{-1}, at the current density of 0.4 A g^{-1}. The reversible charge/discharge lingers between 1140/1135.0 mAh g^{-1} and 1058.8/1051.4 mAh g^{-1}, at the 200th cycle, with a high stability as indicated by CEs between 99.7% and 98.7%. A large average capacity is reinstated after cycling at high rates.

Keywords: Porous $ZnCo_2O_4$ nanorods; Zn defective $ZnCo_2O_4$; Lithium-ion battery

1. Introduction

Novel renewable energy sources and energy storage materials are two major challenges in electrochemical technology. Rechargeable lithium ion batteries (LIBs) with high energy and power density, low cost, and short charging time are recognized as strikingly important devices of power sources to meet the rapid development of the increasing number of portable electronic devices, hybrid and electric vehicles and energy storage systems [1-2]. The electrochemical performance of safe LIBs largely depends on the electrode materials for lithium storage, the current commercial anode (graphite) of LIBs being curbed by the low theoretical capacity (372 mAh g^{-1}) and the limited hosts of Li-ion

ACCEPTED MANUSCRIPT

intercalation [3]. Among the assortment of promising anode materials for LIBs, transition metal oxides (TMOs), such as NiO, SnO_2, Co_3O_4 and Mn_3O_4, have been widely studied on account of their higher specific theoretical capacities and their capability of hosting Li ions in conversion reactions [4,5,6,7,8,9,10,11,12,13,14,15,16,17]. However, most metal oxides undergo large changes in volume during Li^+ insertion and extraction, which leads to the electrode pulverization of anode materials from current collectors, poor electrical conductivity and high voltage plateaus [18,19,20]. As a result, ternary oxides, especially in the AB_2O_4 (A=Mg, Mn, Fe, Co, Ni, Cu, or Zn; B=Mn, Fe, Co, Ni, or Cu), with a variety of crystal structures (spinel, brannerite, scheelite, among the others) have been investigated as anode materials for LIBs [21,22,23,24,25,26,27]. Among them, $ZnCo_2O_4$, is considered as a beckoning candidate, due to the Zn electrochemical activity in Li-ion insertion/extraction [28,29, 30,31,32]. Several methods have been employed to synthesize $ZnCo_2O_4$, resulting in different morphologies, some of them including exogenous supports such as Ni foam or carbon fibers [33,34,35,36,37]. Recently, $ZnCo_2O_4$ for energy storing purposes was obtained by the hydrothermal synthesis in shape of nanoclusters [38], coral-like assemblies of nanorods [39], microspheres [40,41,42] and nanorods [43], whereas coprecipitation was used for flake-by-flake [44] and fiber bundles [45] and a combination of the two methods afforded rod-like nanostructures [46]. Ultrasonic spray pyrolysis yielded yolk-shell $ZnCo_2O_4$ [47]. The associated electrochemical performances range between the high reversible specific capacity of 940 mAh g^{-1} after 100 cycles at 0.1 A g^{-1} of the microspheres [38] to the structure and heat stability of the yolk-shell $ZnCo_2O_4$ at 60°C and 3 A g^{-1} after 200 cycles [45]. In spite of all the progresses achieved, it is enticing to further develop the electrochemical performance of $ZnCo_2O_4$, especially the rate capacity and the cycling stability. A pathway to pursue this purpose is via defective oxides. In general, defects influence the metal oxides electronic structure, charge transport, optoelectronic reactivity and catalytic properties, such as for $M_xCo_{3-x}O_4$ structures, (M=Co, Ni, Zn) where O vacancies play a role in CH_4 and CO oxidation [48] or Co_3O_4 where surface oxygen vacancies influence the formaldehyde oxidation [49]. Recently, defective $ZnCo_2O_4$ nanoparticles, with Zn vacancies have been synthesized and probed as an anode material for LIBs, showing high rate capability and good capacity retention [50]. As morphology clearly plays a role in the efficiency of the electrochemical performances, a synthetic pathway is probed in the current study, to obtain elongated $ZnCo_2O_4$ to be etched in strongly alkaline conditions. The aim is at enhancing the electrochemical response, by possibly introducing a higher porosity in a different morphological structure, in addition to the Zn-vacancy related enhancing of Li^+ insertion/extraction. The synthetic strategy adopted in the current study relies on the shaping effects of a chelating agent such as oxalate in a co-precipitation procedure, aided by the cetyl trimethylammonium bromide (CTAB). The

ACCEPTED MANUSCRIPT

first phase is, then, followed by low-temperature autoclave residence, as broached by Huang et al. [46], calcination and etching. This way, high surface area, porous, Zn-defective $ZnCo_2O_4$ nanorods are obtained which proved to have high electrochemical performances both in terms of rate capacity and of the cycling stability.

2. Experimental

2.1. Material synthesis

The $ZnCo_2O_4$ nanorods were synthesized by co-precipitation followed by hydrothermal treatment and calcination. In the first stage, 12.5 mmol of oxalic acid ($C_2H_2O_4$, Carlo Erba, 99.9%) and 1 mmol of CTAB (Merck, 99%) were dissolved in 50 ml of a mixture of water and N,N dimethyl formamide -DMF- (50:50, *v:v*) heated up to 75°C and kept under vigorous stirring. A second solution was prepared by dissolving 6 mmol of cobalt nitrate ($Co(NO_3)_2{\cdot}6H_2O$, Carlo Erba 99.9%) and 3 mmol of zinc nitrate ($Zn(NO_3)_2 \cdot 6H_2O$, Carlo Erba, 99.9%) in 30 ml of a mixture of water and DMF (50:50, *v:v*) heated up to 75°C and added dropwise to the first solution still kept under stirring. The pH was adjusted to 10 by adding ammonium hydroxide ($NH_3 \cdot H_2O$, Merck, 33%). The resulting slurry was kept under stirring for 1 h at 75°C after turning pale pink. Then, it was transferred into a 250-ml Teflon-lined stainless steel autoclave, which was subsequently heated up to 100 °C for 24 h. The precipitate was collected upon centrifugation, repeatedly washed with water and, then, dried at 110°C for 10 h in an oven. After cooling down to room temperature, a small amount of the precursor was subject to thermogravimetric analysis, whereas the remaining sample was calcined in air, in a tubular oven, at 350°C for 2½ hours, using a temperature ramp of 2°C/min.

The etching was performed by dissolving 8 g of NaOH into 200 ml of water and adding all of the produced $ZnCo_2O_4$, while keeping the solution under stirring at room temperature, for 1h. The resulting defective $ZnCo_2O_4$ was repeatedly washed with water, till neutrality, and dried under vacuum in an oven at 40°C for 24 h.

2.2. Structural and electrochemical characterization

The X-ray powder diffraction (XRD) patterns were obtained on a Shimadzu XRD-6100 X-ray diffractometer with Cu Kα radiation (λ=1.5418 Å) in the 2θ range of 10–70° operated at 35 kV and 30 mA. The elemental analysis was conducted by inductively coupled plasma atomic emission spectroscopy

ACCEPTED MANUSCRIPT

(ICP-AES) (Baird, PS-6). The thermal behavior was characterized by thermogravimetry and differential thermal analysis (TG–DTA)) (Netzsch, 409PC) in air, in the temperature range 30°C – 600°C, at a ramp rate of 5°Cmin^{-1}. The specific surface area was measured with Micromeritics Instrument Corporation TriStar II 3020 using N_2 adsorption–desorption isotherms at -196°C. X-ray photoelectron spectroscopy (XPS) was performed on an ESCALab MKII X-ray photoelectron spectrometer with non-monochromatized Al-Kα X-ray as excitation source. C 1s at 284.6 eV was used for binding energies correction. The morphology was examined by scanning electron microscopy (SEM) with a Zeiss Auriga Field Emission microscope and high-resolution transmission electron microscopy (HR-TEM) on a FEI Tecnai G2 20 high-resolution transmission electron microscope. Electrochemical measurements were carried out on an electrochemical working station (Zennium, Zahner-elektrik).

The working electrode was prepared by very gently mixing 70 wt% of active material (either defective $ZnCo_2O_4$, or non-defective $ZnCo_2O_4$ for comparison purposes) with 20 wt% of acetylene black (ATB) in an agate mortar until a homogeneous powder was obtained, then, 10 wt% polytetrafluoroethylene (PTFE) binder was added together with a few drops of ethanol. The electrolyte (0.1 ml) consisted of 1 mol l^{-1} $LiPF_6$ dissolved in ethylene carbonate (EC), propylene carbonate (PC), and diethyl carbonate (DEC) in the volume ratio of 3:1:1. In each coin cell, the weight of the active material was about 3.0 to3.5 mg. A pure Li foil was used as counter and reference electrode, and a polypropylene (PP) film (Celgard 2400) was used as separator.

3. Results and discussion

TG–DTA was used to determine a suitable calcination temperature to prepare the $ZnCo_2O_4$ powder. The precursor was heated from room temperature up to 600°C at a rate of 5 °C min^{-1} in flowing air atmosphere. From the curves shown in Fig. 1, it can be seen that the TG curve exhibits two distinct weight-loss steps. The first one, by 22.0 %, in the temperature range 80°-150°C can be attributed to the decomposition of the residual organic reagents, to the evaporation of the moisture and of the crystal water in the precursor according to the reaction:

$$ZnCo_2(C_2O_4)_3 \cdot 7H_2O \rightarrow ZnCo_2(C_2O_4)_3 + 7H_2O\uparrow \qquad (1)$$

Correspondingly, a broad endothermic peak appears in the DTA curve. The second weight loss by 37.4% in the temperature range 150°-300°C is associated to a sharp endothermic peak in the DTA curve, and

ACCEPTED MANUSCRIPT

is consistent with the conversion of the anhydrous precursor to $ZnCo_2O_4$ crystals, according to the reaction:

$$ZnCo_2(C_2O_4)_3 + O_2 \rightarrow ZnCo_2O_4 + 4CO_2 \uparrow + 2CO\uparrow \qquad (2)$$

Nearly no weight loss is observed between 330° and 600°C in the TG curve, therefore 350°C was chosen as the lowest calcination temperature still allowing the complete removal of the chelating agent.

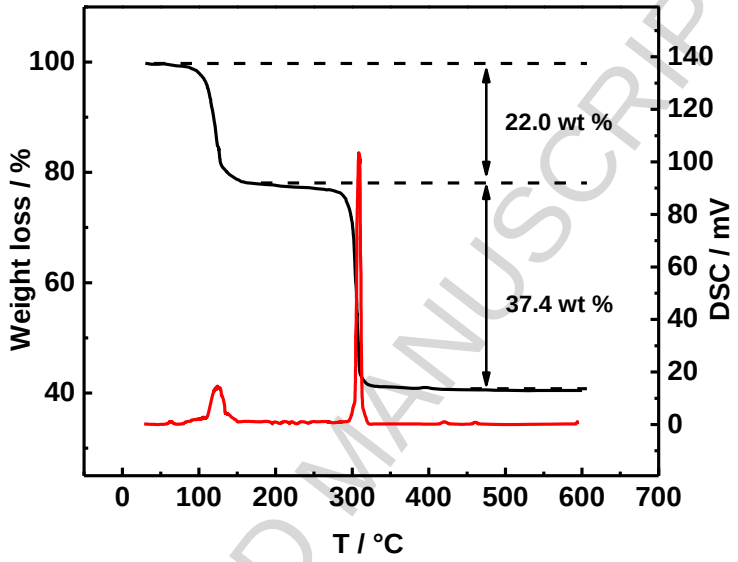

Fig. 1 TGA (── black solid line) and DT(── red solid line) curves for the $ZnCo_2O_4$ precursor.

The sample is, then, etched with NaOH, based on the reactivity of the Zn^{2+} in solid solution to form $Zn(OH)_4^{2-}$ under strongly alkaline conditions, thus aiming at creating Zn-defective $ZnCo_2O_4$ nanorods. The ensuing Zn:Co mole ratio measured by ICP-AES is 0.96:2.00, leading to a formula of $Zn_{0.96}Co_2O_4$. Residual traces of Na^+ are < 10 ppm.

3.1. Structure and morphology of the defective $ZnCo_2O_4$ nanorods

The XRD pattern of the obtained powder is reported in Fig. 2. The diffraction peaks appear at the 2θ values of 18.97°, 31.22°, 36.79°, 38.49°, 44.74°, 55.57°, 59.36°, and 65.13° and correspond to a cubic spinel structure [51] with the divalent Zn ions occupying the tetrahedral sites and the trivalent Co ions occupying the octahedral ones. No spurious phase is detected. Based on the full width at half maximum (FWHM) of the diffraction peak (311), the size of the $ZnCo_2O_4$ grains was estimated to be 15 nm using

ACCEPTED MANUSCRIPT

Scherrer's equation $D = K \lambda / \beta \cos(\theta)$, where D is the average diameter, K is the shape factor usually approximated to 0.9, λ is the used X-ray wavelength, θ is the Bragg angle and β is the pure diffraction broadening of the peak at half-maximum, i.e. the broadening due to the crystallite dimensions.

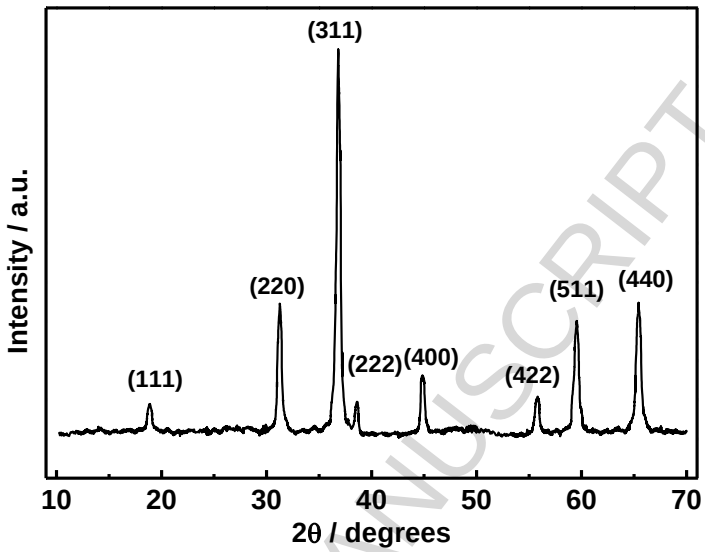

Fig. 2 XRD diffraction pattern of the Zn defective $ZnCo_2O_4$ powder.

The surface chemical composition of the defective $ZnCo_2O_4$ sample is provided by the XPS spectra. In Fig. 3 a wide-scan spectrum is reported (Fig. 3a) along with the spectra in the binding energy ranges of Zn (Fig. 3b), Co (Fig. 3c) and O (Fig. 3d). A deconvolution and fitting of the main peaks was carried out using Gaussian-Lorentzian shaped peaks based on the Shirley background correction. Two major peaks are present at binding energies of 1044.4 eV and 1021.3 eV in the Zn 2p spectrum, attributed to Zn $2p_{1/2}$ and Zn $2p_{3/2}$ which indicate the Zn(II) oxidation state [52-53]. The line-shape analysis of the Zn $2p_{3/2}$ peak pinpoints the presence of a majority component (98.5 atomic %) at 1021.2 eV and traces of a 1.5 atomic % minority component on the high energy side, at 1022.3 eV (i.e. with a chemical shift of 1.1 eV). This is compatible with the presence of Zn(II) in the form of $Zn(OH)_2$ [54,55], probably as residue of the etching procedure. Two strong peaks are observed at 794.5 eV and 779.8 eV for Co $2p_{1/2}$ and Co $2p_{3/2}$, respectively, with a spin-orbit splitting of 15.1 eV. Generally, if the energy gap is larger than 9-10 eV, the Co cation valence is assigned a value of 3+ [56,57], thus confirming the Co(III) oxidation state in the $ZnCo_2O_4$ [58]. However, after refined fitting of the Co $2p_{3/2}$ peak and associated satellite, the appearance of two weak peaks at 781.9 and 797.1 eV demonstrates the coexistence of small amounts of Co(II), which is not uncommon for $ZnCo_2O_4$ structures, as amply reported in literature [37, 59]. In this

ACCEPTED MANUSCRIPT

case, however, it is not possible to infer, on the basis of the XPS analysis alone, whether the Co^{2+} may be related to the presence of $Co(OH)_2$ or other Co(II)-based compounds, such as CoO, because these species share a similar chemical shift [60]. Upon O1s deconvolution, two strong peaks are obtained at 530.1 eV, which corresponds to the metal-oxygen bond, and at 531.5 eV commonly associated with defects, hydroxyls, chemisorbed oxygen, and lattice oxygen on the surface of the spinel structure [61].

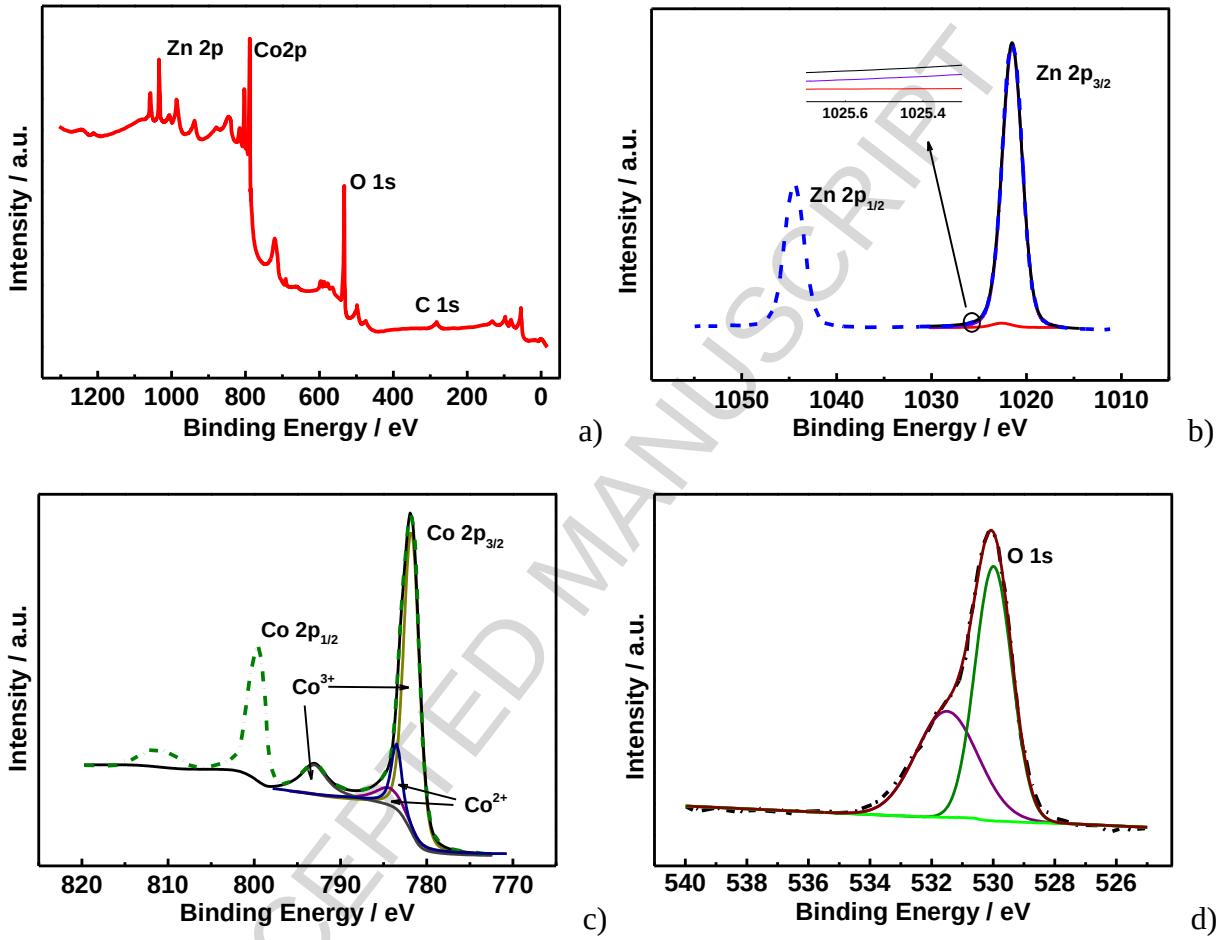

Fig. 3 XPS spectra of the defective $ZnCo_2O_4$ nanorods: a) wide-scan, b) Zn 2p (— · — blue dash-dotted line), along with the line shape analysis of the $2p_{3/2}$ component: Zn^{2+}(—— violet solid line), $Zn(OH)_2$ (—— red solid line), total curve (—— black solid line); c) Co 2p (— · — olive green dash-dotted line), along with the line shape analysis $2p_{3/2}$ component and associated satellite: Co^{3+}(—— dark yellow solid line), Co^{3+} satellite (—— dark gray solid line), Co^{2+} components (—— navy blue and —— purple solid lines), total curve (—— black solid line); and d) O1s spectra (— · — black dash-dotted line), along with line shape analysis: lower binding energy component (—— olive green solid line) associated with the metal oxygen bonds and higher binding energy component (—— violet solid line) associated with defects, total curve (—— wine red solid line); the green solid line (——) is the background.

The advantages of using a CTAB assisted, step-wise synthesis of $ZnCo_2O_4$ can be appreciated in the morphology investigations by SEM and TEM. A SE macrograph of the as-synthesized $ZnCo_2O_4$ is reported in Fig. 4 a) and consists of nanoparticles with an average diameter in the 10-20 nm range,

ACCEPTED MANUSCRIPT

rearranged in tubular super-structures of 80±20 nm diameter (nanorods). The nanorods have a porous structure related to the decomposition of the precursor to $ZnCo_2O_4$: many nanopores with the size up to 10 nm can be observed among the $ZnCo_2O_4$ nanocrystals. Compared to the preparation without CTAB [46], and in overall different synthetic conditions, the current preparation provides smaller nanoparticles [62] and a consequent larger amount of pores at the boundaries among the nanoparticles constituting the nanorods. This has the advantageous consequence of improved electrochemical performances, due to the high specific surface area and confining dimensions effects, which may eschew long diffusion pathway for both Li^+ and e^-, and increase the active sites for Li^+ insertion/extraction reactions [63, 64]. Morphology and particle size are retained after etching (Fig. 4b), thus proving that the treatment does not damage the structure of the nanorods.

In Fig. 4c), the TEM of the etched sample clearly displays the well-dispersed nanorods, composed of $ZnCo_2O_4$ nanocrystals of size and overall average diameters in line with the SE micrographs, connected with each other to form a stable nanostructure.

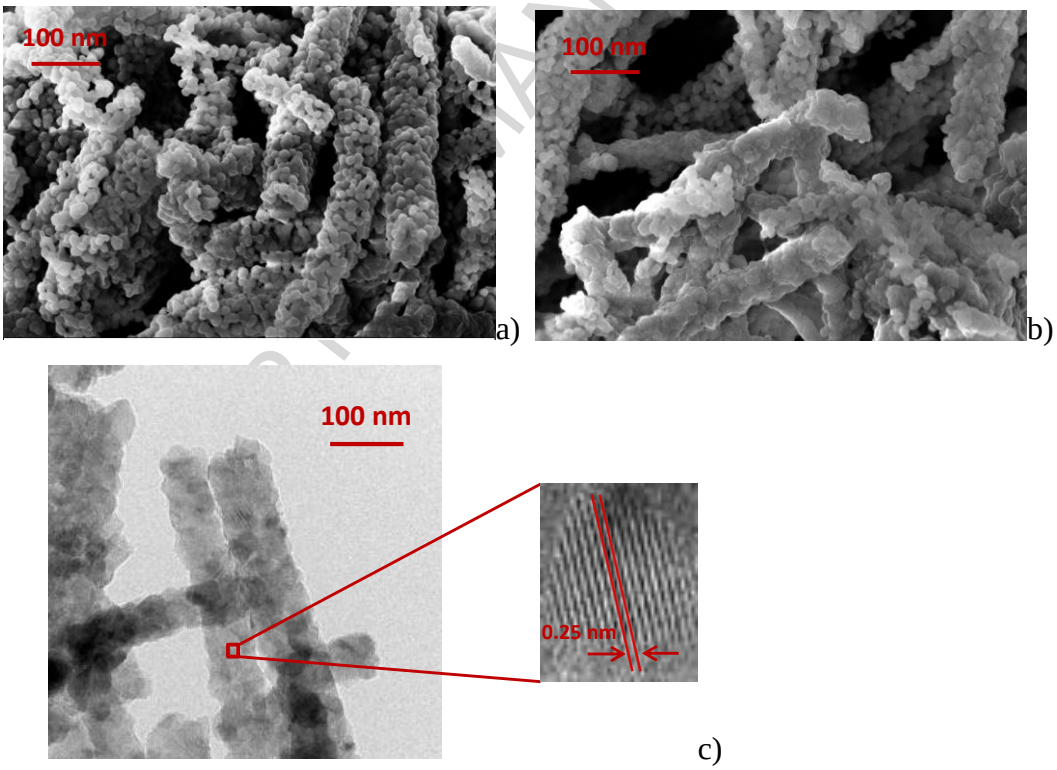

Fig. 4 a) and b) SE micrographs of $ZnCo_2O_4$ nanorods, respectively before and after etching; c) TEM and HR-TEM images of the defective $ZnCo_2O_4$ nanorods.

The magnification of a selected area shows the lattice image of individual $ZnCo_2O_4$ nanocrystals. The lattice fringes with a spacing of 2.5 Å are well matched with the d-values between the (311) planes shown in the XRD pattern.

ACCEPTED MANUSCRIPT

The surface areas of the non-etched and etched samples measured by BET are 170.25 $m^2 g^{-1}$ and 200.15 $m^2 g^{-1}$, respectively. The higher value of the etched sample is probably related to the additional interface due to Zn vacancies in the nanorods.

3.2. Electrochemical performance of the defective $ZnCo_2O_4$ nanorods

The electrochemical performance of the defective $ZnCo_2O_4$ nanorods was investigated to bear out their applicability as LIBs anode material. Cyclic voltammetry provides details on the electrochemical reactions of the defective $ZnCo_2O_4$ nanorods with the electrolyte. Fig. 5a) reports the 1st, 2nd and 8th cyclic voltammograms of the defective $ZnCo_2O_4$ nanorods electrode taken in the potential range 0.005–3.0 V vs. Li/Li^+ at a scan rate of 0.1 mV s^{-1}. The first cathodic wave displays an onset starting at 0.8 V and, then, a sharp peak befalls at 0.5 V, which can be ascribed to the insertion reaction of Li^+ into $ZnCo_2O_4$, the subsequent reduction of Zn^{2+} and Co^{3+} to Zn^0 and Co^0, respectively, according to reaction (3), and the formation of Li–Zn alloys (equation 4). In the anodic sweep, two main oxidation peaks are observed at 1.7 and 2.0 V, corresponding to the electrochemical lithium extraction reactions of equations (5)–(7). The former can be attributed to the concomitant formation of ZnO, the latter to the formation of Co_3O_4 [65,66].

$$ZnCo_2O_4 + 8Li^+ + 8e^- \rightarrow Zn + 2Co + 4Li_2O \quad (3)$$

$$Zn + Li^+ + e^- \rightleftharpoons LiZn \quad (4)$$

$$Zn + Li_2O \rightleftharpoons ZnO + 2Li^+ + 2e^- \quad (5)$$

$$2Co + 2Li_2O \rightleftharpoons 2CoO + 4Li^+ + 4e^- \quad (6)$$

$$2CoO + 2/3\ Li_2O \rightleftharpoons 2/3\ Co_3O_4 + 4/3\ Li^+ + 4/3\ e^- \quad (7)$$

In the 2nd and 8th cycles, the reduction peak initially at around 0.5 V moves to about 0.9 V. The irreversible capacity loss may come from the consumption of active materials in the formation of the solid electrolyte interface (SEI) film and the irreversible reduction reactions [67,68]. The two oxidation peaks have almost no shift and overlap rather well from the 2nd to 8th cycles, indicating good electrochemical reversibility in the lithium insertion and extraction reactions, as well as the stability of the assembled structure. The wee variations between the 2th and the 8th curve can be ascribed to small

ACCEPTED MANUSCRIPT

structural adjustments throughout the cycling, with associated addition/removal of levels in the HOMO-LUMO region of the electrolyte, and consequent small variations the voltage window [69].

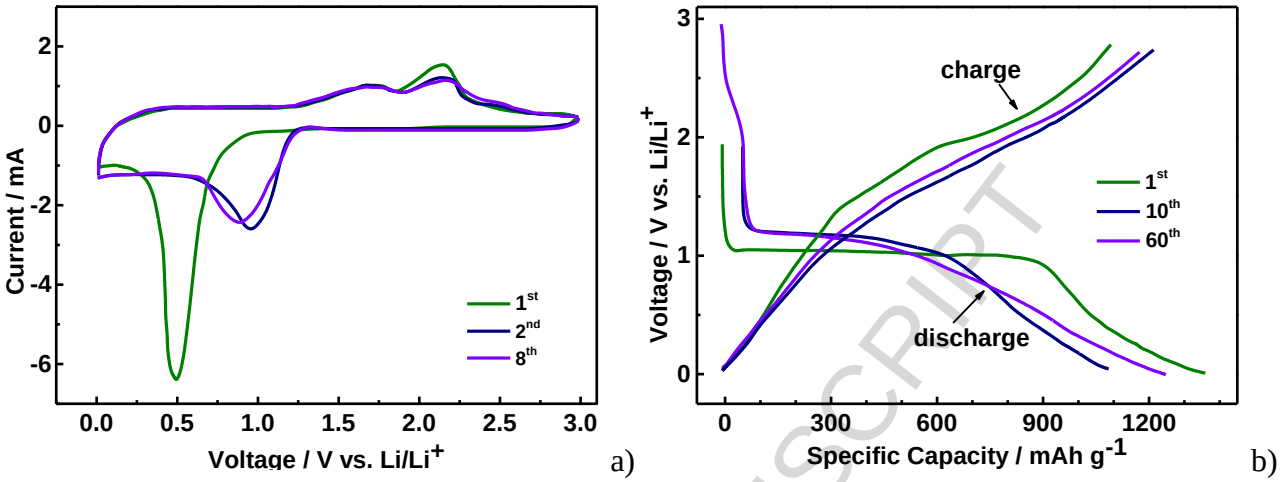

Fig. 5 a) 1st (—— green solid line), 2nd (—— navy blue solid line), and 8th (—— violet solid line) cyclic voltammogram curves of the defective $ZnCo_2O_4$ nanorods electrode at a scan rate of 0.1 mV s^{-1} in the range of 0.01-3.0 V. b**)** Discharge–charge profiles of the defective $ZnCo_2O_4$ nanorods electrode for the 1st (—— green solid line),, 10th (—— navy blue solid line), and 60th (—— violet solid line) cycles at a constant current density of 0.4 A g^{-1}.

The discharge–charge curves of the defective $ZnCo_2O_4$ nanorods electrode at the 1st, 10th and 60th cycles were recorded at a current density of 0.4 A g^{-1} in the voltage range of 0.01–3.0 V (Fig. 5b)). The first discharge curve exhibits a long voltage plateau at 1.0–0.9 V, followed by a sloping down to the cutoff voltage of 0.01 V. Remarkably, also the following cycles produce potential plateaus, though shorter than the 1st one, beginning at about 1.25 V, whereas the gradient of the discharge plateau becomes steeper and steeper as the cycle number increases. The voltage plateaus are well consistent with the peaks in the CV curves.

The cycling performance and the coulombic efficiency of the defective $ZnCo_2O_4$ nanorods electrode are presented in Fig. 6, left panel, at a current density of 0.4 A g^{-1}. The initial discharge specific capacity of the defective $ZnCo_2O_4$ nanorods electrode is 1398.8 mAh g^{-1}, i.e. much higher than the theoretical value of 975 mAh g^{-1}, a phenomenon which can be attributed to the formation of SEI films and organic polymeric/gel-like layer by electrolyte decomposition [70,71].

In addition, interfacial storage originating from the nanorods porous structure is a likely candidate to contribute to the high extra capacity [45,72]. The initial charge specific capacity is 1118.1 mAh g^{-1}, corresponding to a coulombic efficiency (CE) of about 79.9%. The irreversible loss of the initial capacity

ACCEPTED MANUSCRIPT

by 20.1% is well-known and can be related again to the formation of a SEI film on the surface of the active materials [25,26,34,49], the decomposition of the electrolyte, and the reduction of the metal oxides to metals with Li_2O formation [73].

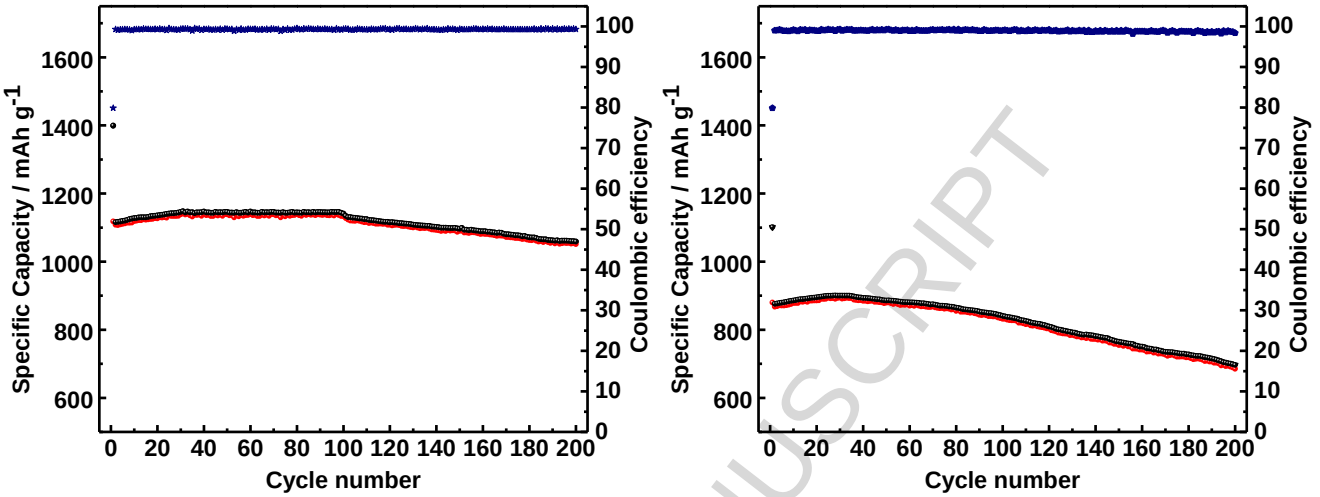

Fig. 6 Cycling performances at 0.4 A g^{-1} for the first 200 cycles. Left panel: defective $ZnCo_2O_4$ electrode, =charging specific capacities, =discharging specific capacities,★=coulombic efficiencies; Right panel: pure $ZnCo_2O_4$ electrode, =charging specific capacities, =discharging specific capacities,▼= coulombic efficiencies.

The reversible capacities of the cycles from the 2nd to the 30th are gradually increasing seemingly for the formation of a polymeric surface film adhering to the active material [21, 25, 45, 46]. Afterwards, the discharge/charge capacity of the defective $ZnCo_2O_4$ nanorods remains very stable and lingers between 1140/1135.0 mAh g^{-1} and 1131/1126 mAh g^{-1}, respectively, up to the 100th cycle. Then, it begins dimming to reach 1058.8/1051.4 mAh g^{-1} at the 200th cycle, as effect of the soaring of continuous loss of active material, low pace embedding of metallic cobalt and zinc into Li_2O matrix, active species aggregation and ineludible structure strain of the electrode materials. The CEs swerve between 99.7% and 98.7% throughout all the cycles demonstrating an overall unordinary high stability of the defective $ZnCo_2O_4$ nanorods, as well as the fast transport paths of Li-ions in $ZnCo_2O_4$. Zn vacancies also play a role in the electrochemical performance and in order to evaluate the extent of their contribution, the discharge/charge capacities of pure (non-defective) $ZnCo_2O_4$ nanorods were measured, for comparison purposes, always at a current density of 0.4 A g^{-1}, as reported in Fig. 6, right panel. It can be noted that pure $ZnCo_2O_4$ nanorods display a lower charge/discharge capacity than the defective ones at the same cycle, suggesting that the Zn vacancies may activate the reaction sites more efficiently [74]. The defects may affect the overall electrochemical performances according to a twofold action. From one side, the

ACCEPTED MANUSCRIPT

Zn vacancies may generate anti-site, off-stoichiometric arrangements in the $ZnCo_2O_4$ structure creating acceptor-donor levels [75, 76, 77], which influence the transport properties. On the other hand, once ZnO is formed upon reaction (5), the electrocatalytic effect of the Zn vacancies, is possibly even more pronounced. The enhancement of electrochemical (and also magnetic and optical) properties in Zn defective ZnO is well-known and largely documented [78,79, 80].

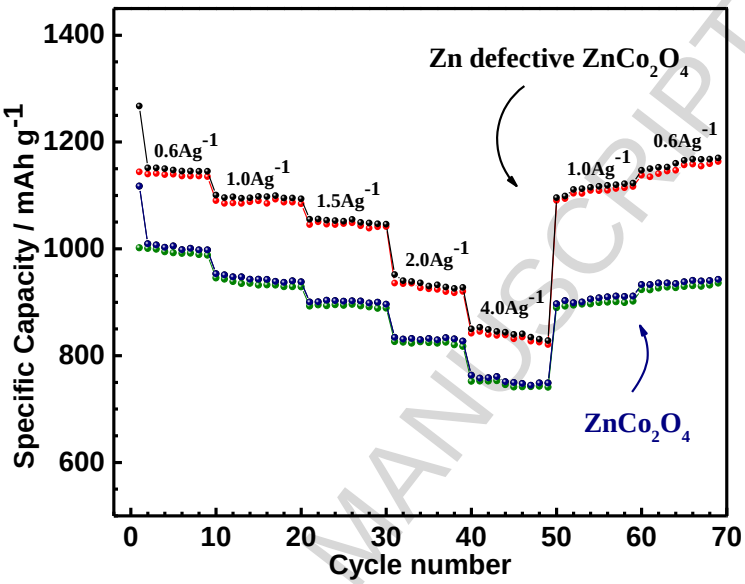

Fig. 7 Rate performances at current densities of 0.6, 1.0, 1.5, 2.0 and 4.0 A g^{-1}. =charging specific capacities and =discharging specific capacities of the defective $ZnCo_2O_4$ nanorods electrodes. = charging specific capacities and =discharging specific capacities non-defective $ZnCo_2O_4$ nanorods electrodes

The initial discharge/charge capacities of 1101.2/879.9 mAh g^{-1} at the 1st cycle, drop to 875.9/870.3 mAh g^{-1} at the 2nd cycle, then increase gradually up to 900.4/894.0 mAh g^{-1} at the 30th cycle.

From this point onward, a constant decrease is observed and the capacities reach 696.5/685.5 mAh g^{-1} after a prolonged cycling up to the 200th cycle. The CEs are 79.9% for the 1st cycle and ranges between 99.6% and 98.4% throughout the other cycles.

To further demonstrate the good performance of the defective $ZnCo_2O_4$ nanorods, the rate capabilities are evaluated by a multiple-step galvanostatic strategy at various current densities in the range 0.6-4.0 A g^{-1} as presented in Fig. 7. The average discharge/charge capacities at 0.6A g^{-1} with the exception of the 1st cycle are 1145.8/1137.61 mAh g^{-1}. When the rate increases up to 4.0 g A^{-1}, the average capacity decreases, but it is remarkably reinstated, when the rate finally returns to 1.0 g A^{-1}, and 0.6 g A^{-1}, after

ACCEPTED MANUSCRIPT

cycling at high rates. This is an indication that a faster Li-ion transfer between electrolyte and electrode is promoted by more Li^+ insertion/extraction and a large interface area. In particular, the specific capacities are 1100.6/1090.2 mAh g^{-1} at 1.0 A g^{-1}, 1055.3/1045.4 mAh g^{-1} at 1.5 A g^{-1}, 951.9/936.0 mAh g^{-1} at 2.0 A g^{-1}, and 850.1/842.0 mAh g^{-1} at 4.0 A g^{-1}. The subsequent increase of the current density back to 1.0 A g^{-1} is characterized by an improvement of the specific capacity up to 1095.4/1088.1 mAh g^{-1} and at 0.6 A g^{-1} it reaches 1147.0/1137.6 mAh g^{-1}. In comparison, the rate capabilities of the non-defective $ZnCo_2O_4$ nanorods are lower, as can be observed also in Fig. 7, and, in particular, the specific capacities at low current densities do not increase after cycling at current densities as high as 4.0 A g^{-1}. The values found for the non-defective $ZnCo_2O_4$ nanorods are 1009.3/1000.9 mAh g^{-1} at the 2nd cycle at 0.6 A g^{-1}, 953.2/945.5 mAh g^{-1} at 1.0 A g^{-1}, 900.1/892.7 mAh g^{-1} at 1.5 A g^{-1}, 834.3/826.2 at 2.0 A g^{-1}, and 763.2/752. 1 mAh g^{-1}, at 4.0 A g^{-1}. The subsequent increase of the current density back to 1.0 A g^{-1} is characterized by a specific capacity of 896.9/889.8 mAh g^{-1} and at 0.6 A g^{-1} it reaches 932.9/923.6 mAh g^{-1}.

The overall performances of the defective nanorods are higher than those reported for Zn defective $ZnCo_2O_4$ nanoparticles with formula $Zn_{0.95}Co_2O_4$ (not re-arranged in any superstructure) and their non-defective counterparts, with similarly built electrodes and in analogous cycling conditions [50]. In the case of the nanoparticles, the specific capacities range between 618.0/608.3 mAh g^{-1} (2nd cycle) at 0.6 A g^{-1} and 158.2/152.6 mAh g^{-1}, at 4.0 A g^{-1} for the defective and 578.3/562.6 mAh g^{-1} at 0.6 A g^{-1} and 44.7/40.5 at 4.0 A g^{-1} for the non-defective $ZnCo_2O_4$ nanoparticles electrodes. Similarly to the defective $ZnCo_2O_4$ nanorods, the specific capacity of the defective nanoparticles increases after cycling at high current density, at variance with the non-defective counterpart. The nanorods and nanoparticles have in common a better performance of the defective with respect to the non-defective correspondent. The higher performances of the defective nanorods over the nanoparticles structures can be ascribed to the different morphologies. In particular, the excellent electrochemical performances of the defective $ZnCo_2O_4$ nanorods can be attributed to their distinct structural properties. Several features concur to determine the electrochemical behavior, related both to the initial $ZnCo_2O_4$ structure and to the etching of the material. The as-prepared nanorods consist of small building blocks of the primary nanoparticles, leading to a very high surface area for the redox reaction. The $ZnCo_2O_4$ nanoparticles are arranged in nanorods with associated mesoporosity, which enhances the electrolyte/electrode contact area for both the surface and inner space, thus facilitating the ion transportation. The etching procedure provides an even larger interface, activates more reaction sites, with consequent faster transport paths for both Li ions and electronics insertion and extraction.

ACCEPTED MANUSCRIPT

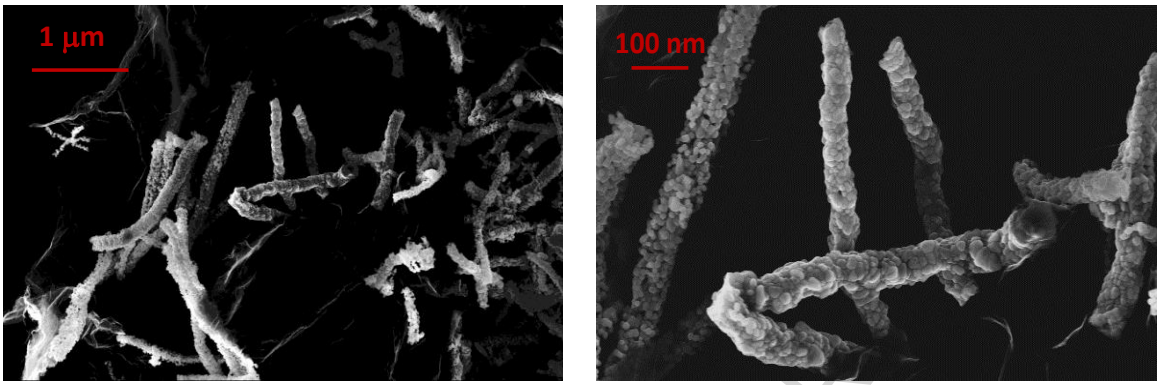

Fig. 8 SE micrographs of the defective $ZnCo_2O_4$ electrode after cycling at 0.4 A g^{-1} 200 times

Finally, Fig. 8 reports the SE micrographs of the defective $ZnCo_2O_4$ electrode after cycling \at 0.4 A g^{-1} 200 times. The tubular rearrangement of the nanoparticles is well preserved, without collapse or molting, thus indicating an excellent structural stability in line with the advanced capacity retention.

4. Conclusions

Defective $ZnCo_2O_4$ nanorods with Zn vacancies were successfully obtained via step-wise synthetic procedure where CTAB assisted co-precipitation is followed by autoclave treatment, calcination and bespoke alkaline etching. $ZnCo_2O_4$ nanorods morphology, porosity and overall structure are retained upon etching, whereas the BET specific surface is, instead, larger. The initial discharge capacity is 1398.8 mAh g^{-1} at 0.4 A g^{-1}. Then, the reversible charge/discharge capacity lingers between 1140/1135.0 mAh g^{-1} and 1058.8/1051.4 mAh g^{-1}, at the 200th cycle, with a high stability as indicated by CEs between 99.7% and 98.7%. A large average capacity is reinstated after cycling at high rates, indicating a faster Li-ion transfer between electrolyte and electrode, promoted by more Li^+ insertion/extraction and a large interface area. This effect, along with higher charge/discharge capabilities are even more pronounced than with defective $ZnCo_2O_4$ nanoparticles, indicating a shape-effect of porous nanorods on the overall electrochemical process.

ACCEPTED MANUSCRIPT

References

[1] Y. Zhao, L.P. Wang, M.T. Sougrati, Z. Feng, Y. Leconte, A. Fisher, M. Srinivasan, Z. Xu, Adv. Energy Mater 7 (2017) 1601424 (1-70).
[2] X.Y. Guo, X. Cao, G.Y. Huang, Q.H. Tian, H.Y. Sun, J. Environ. Manag. 198 (2017) 84-89.
[3] B. Scrosati, J. Garche, J. Power Sources 195 (2010) 2419-2430.
[4] S. Abouali, M.A. Garakani, Z.L. Xu, J.K. Kim, Carbon 102 (2016) 262-272.
[5] G.Y. Huang, S.M. Xu, Y. Yang, H.Y. Sun, Z.H. Xu, RSC Adv. 6 (2016) 10763-10774.
[6] V. Etacheri, R. Marom, R. Elazari, G. Salitra, D. Aurbach, Energy Environ. Sci. 4 (2011) 3243-3262.
[7] G.Y. Huang, S.M. Xu, Y. Yang, Y.B. Cheng, J. Li, Chin. J. Inorg. Chem. 32 (2016) 1693-1703.
[8] J. Mujtaba, H.Y. Sun, G.Y. Huang, Y.Y. Zhao, H. Arandiyan, G.Y. Sun, S.M. Xu, J. Zhu, RSC Adv. 6 (2016) 31775-31781.
[9] M. Carbone, E. Bauer, L. Micheli, M. Missori, Colloid Surface A, 532 (2017) 178-182.
[10] P. Poizot, S. Laruelle, S. Grugeon, L. Dupont, J.M. Tarascon, Nature 407 (2000) 496-499.
[11] G.Y. Huang, S.M. Xu, Y. Yang, Y.B. Chen, Z.B. Li, Int. J. Electrochem. Sci. 10 (2015) 10587-10596.
[12] F. Valentini, D. Roscioli, M. Carbone, V. Conte, B. Floris, G. Palleschi, R. Flammini, E.M. Bauer, Nasillo, E. Caponetti, Anal. Chem. 84 (2012) 5823-5831.
[13] G.Y. Huang, S.M. Xu, Y.B. Cheng, W.J. Zhang, J. Li, X.H. Kang, Int. J. Electrochem. Sci. 10 (2015) 2594-2601.
[14] J. W. Lang, L. B. Kong, W. J. Wu, Y. C. Luo and L. Kang, Chem. Commun. (2008) 4213-4215.
[15] R. K. Selvan, I. Perelshtein, N. Perkas and A. Gedanken, J. Phys. Chem. C, 112 (2008) 1825-1830.
[16] M. Carbone, A. Nesticò, N. Bellucci, L. Micheli, G. Palleschi, Electrochim. Acta, 246 (2017) 580-587.
[17] B. Wang, T. Zhu, H. B. Wu, R. Xu, J. S. Chen and X. W. Lou, Nanoscale, 4 (2012) 2145-2149.
[18] S. Yang, Y. Sun, L. Chen, Y. Hernandez, X. Feng, K. Müllen, Sci. Rep. 2 (2012) 427.
[19] Z. S. Wu, W. C. Ren, L. Wen, L. B. Gao, J. P. Zhao, Z. P. Chen, G. M. Zhou, F. Li, H. M. Cheng, ACS Nano 4 (2010) 3187-3194.
[20] G. M. Zhou, D. W. Wang, F. Li, L. L. Zhang, N. Li, Z. S. Wu, L. Wen, G. Q. Lu, H. M. Cheng, Chem. Mater. 22 (2010) 5306-5313.
[21] M.V. Reddy, G.V. Subba Rao, B.V. Chowdari, Chem. Rev. 113(7) (2013) 5364–5457.
[22] M. Carbone, G. Sabbatella, S. Antonaroli, H. Remita, V. Orlando, S. Biagioni, A. Nucara, Biochim. Biophys. Acta, gen-subj. 1850 (2015) 2304-2307.
[23] Y. Xiao, X. Li, J. Zai, K. Wang, Y. Gong, B. Li, Q. Han, X. Qian, Nano-Micro Lett. 6(4), (2014) 307–315.
[24] M. Carbone, J. Alloy Compd, 688 (2016) 202-209.
[25] Y. Pan, Y. Zhang, X. Wei, C. Yuan, J. Yin, D. Cao, G. Wang, Electrochim. Acta 109 (2013) 89–94.
[26] D. Zhao, Y. Wang, Y. Zhang, Nano-Micro Lett. 3(1) (2011) 62–71.
[27] M. Carbone, R. Briancesco, L. Bonadonna, Environ. Nanotechnol. Monit. Manage. 7 (2017) 97-102.

ACCEPTED MANUSCRIPT

[28] J.W. Jung, C.L. Lee, S. Yu, I.D. Kim, J. Mater. Chem. A 4 (2016) 703-750.
[29] Q. Ru, X. Song, Y.D. Mo, L.Y. Guo, S.J. Hu, J. Alloy. Compd. 654 (2016) 586-592.
[30] S.J. Hao, B.W. Zhang, S. Ball, M. Copley, Z.C. Xu, M. Srinivasan, K. Zhou, S. Mhaisalkar, Y.Z. Huang, J. Power Sources 294 (2015) 112-119.
[31] A.K. Rai, T.V. Thi, B.J. Paul, J. Kim, Electrochim. Acta 146 (2014) 577-584.
[32] C.W. Lee, S.D. Seo, D.W. Kim, S. Park, K. Jin, D.W. Kim, K.S. Hong, Nano Res. 6 (2013) 348-355.
[33] Y. Pan, H. Gao, M. Zhang, L. Li, Z. Wang, J. Alloy. Compd. 702 (2017) 381-387.
[34] B. Qu, L. Hu, Q. Li, Y. Wang, L. Chen, T. Wang, ACS Appl. Mater. Interfaces 6 (2014) 733-736.
[35] S. Wang, J. Pu, Y. Tong, Y. Cheng, Y. Gao, Z. Wang, J. Mater. Chem. A 2 (2014) 5434-5440
[36] X. Hou, S. Bai, S. Xue, X. Shang, Y. Fu, D. He, J. Alloy. Compd. 711 (2017) 592-597.
[37] B. Liu, J. Zhang, X. Wang, G. Chen, D. Chen, C. Zhou, G. Shen, Nano Lett. 12 (2012) 3005-3011.
[38] Y. Pan, W. Zeng, L. Li, Y. Zhang, Y. Dong, D. Cao, G. Wang, B.L. Lucht, K. Ye, K. Cheng, Nano-Micro Lett. 9 (2017) 20.
[39] J.A. Rajesh, B.-K. Min, J.-H. Kim, S.-H. Kang, H. Kim, K.-S. Ahn, J. Electroanal. Chem. 785 (2017) 48–57.
[40] S. Hao, B. Zhang, S. Ball, M. Copley, Z. Xu, M. Srinivasan, K. Zhou, S. Mhaisalkar, Y. Huang, J. Power Sources 294 (2015) 112-119.
[41] Q. Wang, L. Zhu, L, Sun, Y. Liu, L. Jiao, J. Mater. Chem. A 3 (2015) 982-985.
[42] J. A. Rajesh, B.-K. Min, J.-H. Kim, H. Kim, K.-S. Ahn, J. Electrochem. Soc. 163(10) (2016) A2418-A2427.
[43] H. Liu, J. Wang, Electrochim. Acta 92 (2013) 371– 375.
[44] X. Song, Q. Ru, B. Zhang, J. Alloy. Compd, 585 (2014) 518–522.
[45] X. Song, Q. Ru, Y. Mo, S. Hu, B. An, J. Alloy. Compd. 606 (2014) 219–225.
[46] T. Huang, C. Zhao, R. Zheng, Y. Zhang, Z. Hu, Ionics 21 (2015) 3109–3115.
[47] S. Ho Choi, Y.C. Kang, Yolk–Shell, ChemSusChem 6(11) (2013) 2111–2116.
[48] Z. Ren, V. Botu, S. Wang, Y. Meng, W. Song, Y. Guo, R. Ramprasad, Steven L. Sui, P.-X. Gao, Angew. Chem. Int. Ed. 53 (2014) 7223–7227.
[49] Z. Wang, W. Wang, L. Zhang and Dong Jiang, Catal. Sci. Technol. 6 (2016) 3845-3853.
[50] G. Huang, Y. Yang, H. Sun, S. Xu, J. Wang, M. Ahmad, Z. Xu, J. Alloy. Compd. 724 (2017) 1149-1156.
[51] JCPDS 23-1390.
[52] X.L. Wen, Z. Chen, E.H. Liu, X. Lin, App. Surf. Sci. 35-7 (2015) 1212–1216.
[53] W. Luo, X. Hu, Y. Sun, Y. Huang, J. Mater. Chem. 22 (2012) 8916-8921.
[54] X. Yan, L. Chai, Q. Li, L. Ye, B. Yang, Q. Wang, Cryst. Eng. Comm. 18 (2016) 924-929.
[55] S. Sepulveda-Guzmana, B. Reeja-Jayanc, E. de la Rosa, A. Torres-Castro, V. Gonzalez-Gonzalez M. Jose-Yacaman, Mater. Chem. Phys. 115 (2009) 172–178.
[56] A. Gulino, G. Fiorito, I. Fragala, J. Mater. Chem. 13 (2003) 861-865.
[57] W F. Wei, W.X. Chen, D.G. Ivey, Chem. Mater. 20 (2008) 1941-1947.
[58] I.K. Moon, S. Yoon, J. Oh, Chem. Eur. J. 23 (2017) 597-604.
[59] J. Bai, X. Li, G. Liu, Y. Qian, S. Xiong, Adv. Funct. Mater. 24 (2014) 3012-3020.
[60] M.C. Biesinger, B.P. Payne, A.P. Grosvenor, L.W.M. Lau, A. R. Gerson, R.St.C. Smart, App. Surf. Sci. 257 (2011) 2117-2130.
[61] L. Hu, B. Qu, C. Li, Y. Chen, L. Mei, D. Lei, L. Chen, Q. Li, T. Wang, J. Mater. Chem. A 1, (2013) 5596-5602.
[62] The average size of the nanoparticles in reference [46] is estimated 70nm on visual inspection of Fig. 3d.

ACCEPTED MANUSCRIPT

[63] P.L. Taberna, S. Mitra, P. Poizot, P. Simon, J.M. Tarascon, Nature Mater. 5 (2006) 567–573.
[64] Q.T. Qu, L.J. Fu, X.Y. Zhan, D. Samuelis, J. Maier, L. Li, S. Tian, Z.H. Li, Y.P. Wu, Energy Environ. Sci. 4 (2011) 3985–3990.
[65] H.C. Liu, S.K. Yen, J. Power Sources 166 (2007) 478–484.
[66] C.Q. Zhang, J.P. Tu, Y.F. Yuan, X.H. Huang, X.T. Chen, F. Mao, J. Electrochem. Soc. 154 (2007) 65–69.
[67] L.C. Fernandez, F. Mueller, S. Passerini, L.J. Hardwick, Chem. Commun. 52 (2016) 3970-3973.
[68] B. Liu, J. Zhang, X. Wang, G. Chen, D. Chen, C. Zhou, G. Shen, Nano Lett. 12 (2012) 3005–3011.
[69] C. Liu, Z.G. Neale, G. Cao, ACS Appl. Mater. Interfaces 6 (2014) 733-736.
[70] N. Munichandraiaha, L.G. Scanlonb, R.Amarshb, J. Power Sources 72 (1998) 203-210.
[71] S. Laruelle, S. Grugeon, P. Poizot, M. Dolle, L. Dupont, J.M. Tarascon, J. Electrochem. Soc. 149 (2002) A627–A634.
[72] P. Balaya, H. Li, L. Kienle, J. Maier, J. Adv. Funct. Mater. 13 (2003) 621–625.
[73] D. Deng, J.Y. Lee, Nanotechnology 22 (2011) 355401–355409.
[74] H.J. Park, J. Kim, N.J. Choi, H. Song, D.S. Lee, ACS Appl. Mater. Interfaces 8 (2016) 3233-3240.
[75] F. Zasada, J. Gryboś, P. Indyka, W. Piskorz, J. Kaczmarczyk, Z. Sojka, J. Chem. Phys. C, 118 (2014) 19085−19097.
[76] T.R. Paudel, A. Zakutayev, S. Lany, M. d'Avezac, A. Zunger, Adv. Funct. Mater. 21 (2011) 4493–4501.
[77] Y. Shi, P.F. Ndione, L.Y. Lim, D. Sokaras, T.-C. Weng, A.R. Nagaraja, A.G. Karydas, J.D. Perkins, T.O. Mason, D.S. Ginley, A. Zunger, M.F. Toney, Chem. Mater. 26 (2014) 1867-1873.
[78] G.Z. Xing, Y.H. Lu, Y.F. Tian, J.B. Yi, C.C. Lim, Y.F. Li, G.P. Li, D.D. Wang, B. Yao, J. Ding, Y.P. Feng, T. Wu, AIP Adv. 1 (2011) 22152.
[79] A. Renaud, L. Cario, X. Rocquefelte, P. Deniard, E. Gautron, E. Faulques, T. Das, F. Cheviré, F. Tessier, S. Jobic, Sci. Rep. 5 (2015) 12914.
[80] F. Tuomisto, V. Ranki, K. Saarinen, D.C, Phys. Rev. Lett. 91 (2003) 205502.

ACCEPTED MANUSCRIPT

ACCEPTED MANUSCRIPT

Graphical Abstract

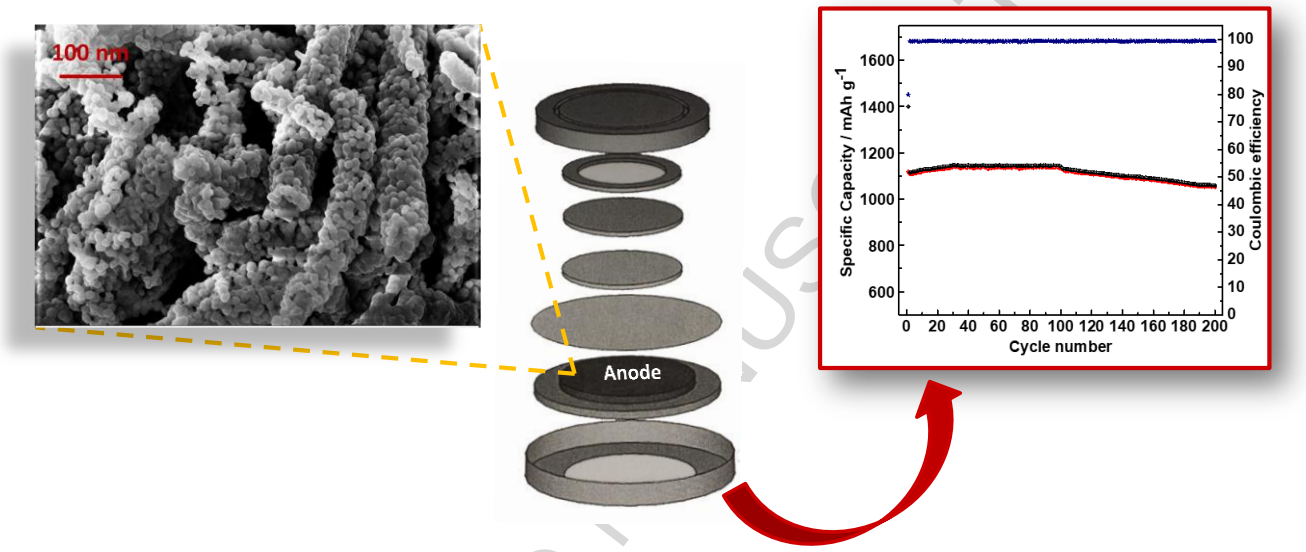

Highlights

- Zn defective $ZnCo_2O_4$ nanorods are synthesized by a stepwise synthetic procedure and tailored etching
- Zn defective $ZnCo_2O_4$ nanorods display a high surface-area porous structure
- Zn defective $ZnCo_2O_4$ nanorods show high specific capacity and high stability as LIB anode material
- After cycling at high rates, the charge/discharge capacities of the Zn defective $ZnCo_2O_4$ nanorods electrode are of the reinstated to 1095.4/1088.1 mAh g^{-1} when the rate is set back to 0.4 A g^{-1}